



OPEN

pentahexoctite: A new two-dimensional allotrope of carbon

Babu Ram Sharma^{1*}, Aaditya Manjanath^{1,2*} & Abhishek K. Singh¹¹Materials Research Centre, Indian Institute of Science, Bangalore-560012, ²Centre for Nano Science and Engineering, Indian Institute of Science, Bangalore-560012.

SUBJECT AREAS:

TWO-DIMENSIONAL
MATERIALSELECTRONIC PROPERTIES AND
MATERIALS

Received

19 September 2014

Accepted

3 November 2014

Published

24 November 2014

Correspondence and
requests for materials
should be addressed to
A.K.S. (abhishek@mrc.
iisc.ernet.in)

* These authors
contributed equally to
this work.

The ability of carbon to exist in many forms across dimensions has spawned search in exploring newer allotropes consisting of either, different networks of polygons or rings. While research on various 3D phases of carbon has been extensive, 2D allotropes formed from stable rings are yet to be unearthed. Here, we report a new sp^2 hybridized two-dimensional allotrope consisting of continuous 5–6–8 rings of carbon atoms, named as “pentahexoctite”. The absence of unstable modes in the phonon spectra ensures the stability of the planar sheet. Furthermore, this sheet has mechanical strength comparable to graphene. Electronically, the sheet is metallic with direction-dependent flat and dispersive bands at the Fermi level ensuring highly anisotropic transport properties. This sheet serves as a precursor for stable 1D nanotubes with chirality-dependent electronic and mechanical properties. With these unique properties, this sheet becomes another exciting addition to the family of robust novel 2D allotropes of carbon.

Carbon has been known to form many allotropes because of its ability to exist in different hybridizations. Among these, the most extensively studied, is graphene¹, a monolayer of sp^2 hybridized carbon atoms. It is a building block for carbon materials such as the three-dimensional (3D) graphite, one-dimensional (1D) carbon nanotubes, and zero-dimensional (0D) fullerenes², all of them exhibiting unique properties. Success of graphene has motivated the search for newer forms of 2D materials. This resulted into finding of various 2D allotropes such as graphyne^{3–12}, graphdiyne^{13,14}, graphenylene¹⁵, biphenylene¹⁶, radialenes^{17–19}, pentaheptite²⁰ and haeckelites²¹. The carbon atoms in these allotropes are either sp^2 and/or sp hybridized. Graphyne (graphdiyne) consists of a network of carbon atoms with one (two) acetylenic linkages between hexagons^{4,5,13,14}. In graphenylene and biphenylene, the arrangement is in the form of squares, hexagons, and octagons (biphenylene)^{15,16}. Radialenes are formed by inserting acetylenic linkages between methylene pairs¹⁷. On the other hand, sheets consisting of 5–7 defects such as pentaheptite and haeckelite are formed by the Stone-Wales transformation²² of bonds in a certain sequence^{20,21}. Interestingly, all these allotropes are planar and exhibit unique electronic as well as mechanical properties.

In addition to the geometric stability of 5–7 rings, 5–8 rings have also been proved to be stable. 1D metallic wires made out of a 5–8 chain in graphene²³ have been shown to be promising for valleytronic devices²⁴. Motivated by the unique nature of this 5–8 line defect in graphene, we explored the possibility of its 2D analog. Here, we report “pentahexoctite”, a sheet consisting of a network of pentagons, hexagons and octagons. The planar stability of the sheet is ensured through the absence of unstable modes in the phonon spectra. The mechanical strength of the sheet is comparable to graphene. Electronic structure shows this sheet to be metallic with a combination of flat and dispersive bands at the Fermi level. The sheet can be rolled into stable nanotubes with chirality-dependent mechanical and electronic properties. These novel properties of the pentahexoctite sheet make it a potential candidate for nanoelectronics devices.

Results and Discussion

Pentahexoctite sheet. The pentahexoctite sheet has two pentagons that are mirror images of each other, surrounded by four octagons and two hexagons as shown in Fig. 1(a). This 2D lattice has a space group of Cmm , (two mirror planes represented by the purple-dashed lines in Fig. 1(a)) with no inversion symmetry. The reduction in symmetry compared to graphene results in anisotropy, which plays a role in determining physical properties. The optimized lattice parameters are $a_1 = 5.85 \text{ \AA}$ and $a_2 = 3.78 \text{ \AA}$ (thick green arrows in Fig. 1(a)). The hexagons in this sheet are not regular and contain two types of angles, i.e. $\alpha = 138.8^\circ$ and $\beta = 110.6^\circ$ (Fig. 1(a)). However, the bond lengths ($a = 1.43 \text{ \AA}$, $b = 1.37 \text{ \AA}$, $c = 1.49 \text{ \AA}$, $d = 1.41 \text{ \AA}$, and $e = 1.39 \text{ \AA}$, in the order specified in Fig. 1(a)) of the neighboring C atoms do not deviate significantly from the sp^2 hybridized bond length of

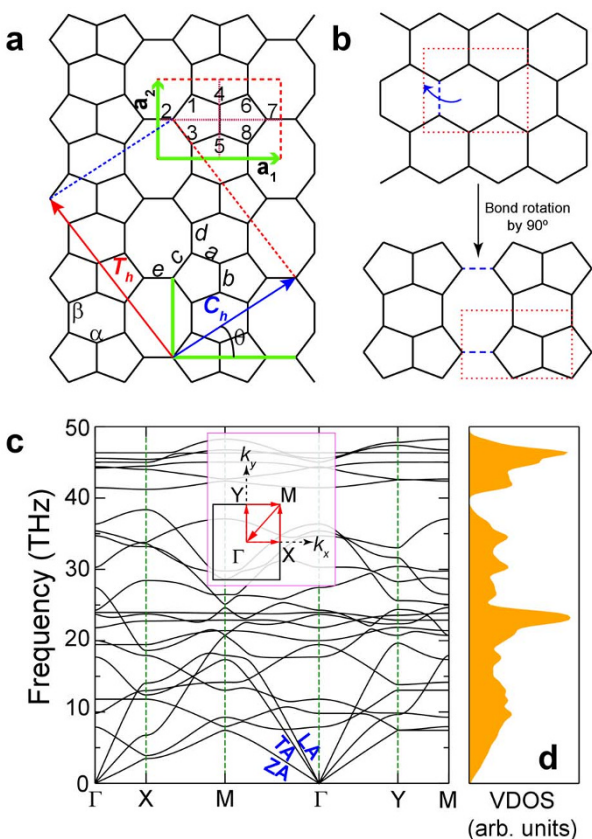


Figure 1 | Geometry and mechanical stability of the pentahexoctite sheet.

(a) The pentahexoctite sheet constructed from the unit cell (red-dashed line) of 8 atoms, with the lattice vectors \mathbf{a}_1 and \mathbf{a}_2 (thick green arrows). The purple-dashed lines represent the mirror planes of symmetry. The bond angles (α and β) of the hexagon, and bond lengths (a , b , c , d , and e) are indicated. The chiral vector \mathbf{C}_h (blue arrow) and the corresponding orthogonal translation vector \mathbf{T}_h , along with the chiral angle (θ) are drawn in the bottom portion of the sheet. (b) A sequential Stone-Wales transformation of graphene (blue-colored bond with the direction of rotation represented by an arrow) leads to this sheet (minimum unit cell required for this transformation is shown as a red-dashed line). (c) Shows the phonon dispersion of the sheet along the symmetry directions given by the 2D rectangular Brillouin zone (inset). The acoustical phonon branches; out-of-plane (ZA), transverse in-plane (TA) and longitudinal (LA); are labeled accordingly in (c). (d) The vibrational density of states (VDOS) of the sheet.

graphene (1.42 Å), more or less preserving the sp^2 hybridization in this sheet. The structure of this sheet can also be derived from graphene by the SW transformation of one of the bonds (blue-colored) in a rectangular unit cell as shown in Fig. 1(b), followed by a complete relaxation of the unit cell including the lattice vectors.

In order to verify the integrity of the planar structure, it was distorted by moving the atoms out of plane in a larger supercell. Upon complete relaxation, the atoms returned to their original positions and the sheet remained planar. Stability of the sheet was further confirmed by calculating the phonon dispersion curve along the high symmetry directions as shown in the inset. There were no negative frequencies observed in the phonon spectra (Fig. 1(c)) and vibrational density of states (VDOS) (Fig. 1(d)). In addition, there is a phononic gap in the neighborhood of 40 THz suggesting its possible application in phononic devices.

Based on the phonon spectra, we also analyze the thermal transport of this sheet. The trends in the lattice thermal conductivity can be found by calculating the group velocities of the longitudinal and

transverse acoustical (LA and TA) modes and comparing these with graphene. The LA group velocity ($v_{LA} \approx 17400 \text{ ms}^{-1}$) is higher compared to the TA velocity ($v_{TA} \approx 5600 \text{ ms}^{-1}$). In addition, v_{LA} of the sheet has comparable magnitude with v_{LA} of graphene ($\sim 21300 \text{ ms}^{-1}$)²⁵, whereas, v_{TA} is lower than graphene's ($\sim 13600 \text{ ms}^{-1}$)²⁵. The out-of-plane modes (ZA) do not contribute significantly to the lattice thermal conductivity, due to negligibly small group velocities, similar to graphene²⁶.

We estimate the lattice thermal conductivity at room temperature assuming the transport to be ballistic in nature. This assumption was based on two observations: i) The temperature considered is much lower than the calculated Debye temperature of this sheet (1229 K). ii) The sheet is highly symmetric having phonon group velocities comparable to graphene. Therefore, the sheet is expected to have long mean-free paths. We employed the Landauer's formalism as implemented in the BallTran code²⁷, to obtain the lattice thermal conductivity of pentahexoctite sheet at room temperature. Due to the inherent structural anisotropy in the sheet, thermal transport is anisotropic. The thermal conductivities along x - and y -directions were $0.741\kappa_0$ and $0.598\kappa_0$, where κ_0 is the thermal conductivity of graphene. This difference arises from the higher value of the LA group velocity compared to that of the TA mode. The overall thermal conductivity of the sheet is lower than that of graphene due to reduced symmetry compared to graphene and increased mixing of the acoustical and optical modes (Fig. 1(c)).

Next, we estimate the mechanical strength of this sheet by calculating the in-plane stiffness C_s which is the double derivative of total energy (E) with respect to atomic displacement (u_x , along α^{th} direction) in the following second-order Taylor series expansion around equilibrium:

$$E = E_0 + \sum_x \frac{\partial E}{\partial u_x} u_x + \sum_{x,\beta} \frac{1}{2} \frac{\partial^2 E}{\partial u_x \partial u_\beta} u_x u_\beta + O(u^3) \quad (1)$$

where, E_0 is the equilibrium energy per atom. This expansion is written in terms of applied strain:

$$\epsilon = \frac{a - a_0}{a_0} \quad (2)$$

with a and a_0 , the lattice parameters with and without strain, respectively, to obtain the equation of C_s :

$$C_s = \frac{1}{A_0} \frac{\partial^2 E(\epsilon)}{\partial \epsilon^2} \quad (3)$$

where, A_0 is the equilibrium area of the sheet per atom and $E(\epsilon)$ is the strain energy per atom.

The C_s value is computed by plotting the strain energy per atom ($E(\epsilon)$) vs. applied strain (ϵ), and fitting this curve to a second-order polynomial of the form:

$$E(\epsilon) = E_0 + \tilde{C}_1 \epsilon + \tilde{C}_2 \epsilon^2 \quad (4)$$

where, E_0 is the equilibrium energy. Using the value of \tilde{C}_2 , C_s is calculated by substituting $\frac{\partial^2 E(\epsilon)}{\partial \epsilon^2}$ with \tilde{C}_2 in equation 3.

The strains were applied along the x - (x -axial strain) and y -axes (y -axial strain) and their corresponding C_s values were found to be 299.4 Nm^{-1} and 338.79 Nm^{-1} , respectively. They differ along these directions due to anisotropy in the sheet. Surprisingly, despite the presence of the pentagonal and octagonal rings, these values are similar to that of graphene²⁸. Hence, the overall mechanical strength of this sheet is comparable with graphene.

To explore the feasibility of the experimental synthesis of this sheet, we compare its energy with the existing 2D allotropes. Fig. 2 shows the relative energy (E_R) of various 2D sheets, with respect to graphene. Incidentally, an interesting trend in energy is observed

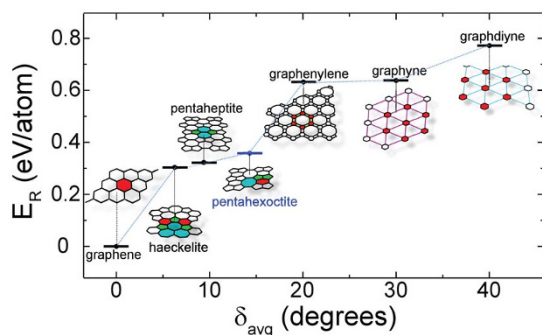


Figure 2 | Relative energy (E_R) of the various 2D allotropes of carbon with respect to pristine graphene as a function of average bond angle deviation (δ_{avg}). The colors indicate the different rings present in each structure.

with respect to the average bond angle deviation (δ_{avg}) from that of graphene (120°). With the increase in δ_{avg} , E_R increases, albeit in a non-linear fashion. This is due to the increased amount of energy required to distort the angles from sp^2 hybridization. The relative energy of pentahexoctite (marked in blue in Fig. 2) is comparable with that of the haeckelite and pentaheptite structures²¹, while it is remarkably lower than graphenylene²⁹, graphyne (magenta bonds)²⁹, and graphdiyne (cyan bonds)³⁰. Despite the high energies of graphyne and graphenylene, they have been successfully synthesized^{12,13}. Furthermore, graphene containing high concentrations of haeckelite rings, and 4–8 rings, have been synthesized using electron irradiation techniques³¹. Recent experimental studies have also reported that irradiation of the graphene sheet by an electron beam of 80 keV (during TEM imaging of the sheet) transfers a maximum energy of 15.6 eV³² to a carbon atom which is below the threshold knock-on voltage of 18–20 eV³¹. This transfer of high energy facilitates the formation of multiple Stone-Wales (SW) defects³², surmounting the SW barrier of 10 eV³³. However, an exposure of this electron beam for very short durations concentrated over a small area (electron dosage of the order of $1 \times 10^{10} \text{ e}^-/\text{nm}^2$)³¹, can lead to immediate (few seconds³²) relaxation to the unperturbed graphene sheet. A strategy of controlled exposure of the pristine graphene sheet to the 80 keV electron beam, along a particular direction for a longer duration over a large area may be employed to obtain the sheet.

Next, we calculate the electronic properties of this sheet. Fig. 3(a) shows the band structure along with the angular momentum resolved density of states (LDOS). The atomic quadruple (1,3,6,8), for instance, exhibits equivalent LDOS as they are connected by the two mirror planes. Similar is the case with the doubles (2,7) and (4,5). Overall, electronically, there are 3 non-equivalent atoms, therefore, the LDOS projected on atoms 1, 2 and 4 are shown in Fig. 3(a). Interestingly, the electronic structure shows a combination of flat and dispersive bands with a finite number of states at the Fermi level (E_F), rendering it metallic. The p_z orbitals of the atoms belonging to the pentagonal and octagonal rings contribute to these states (LDOS of Fig. 3(a)). A similar behavior is observed in 5–8 line defects, and in pentaheptite and haeckelite sheets^{21,23}.

In order to understand the origin of the flat and dispersive bands, the band-decomposed charge density was calculated at $\Delta = (0.25, 0.00, 0.00)$ (Fig. 3(b)) and X points (Fig. 3(c)), respectively. At Δ , the electron density around the atoms belonging to the pentagonal rings are localized. The localized states are due to the limited p_z interactions between these atoms, leading to a flat band. Whereas, at the X point, however, the charge density is delocalized, leading to a dispersive band. The difference in the nature of the bands along different directions, indicates anisotropy in electronic transport.

Pentahexoctite nanotubes. This sheet can also serve as a precursor for materials of different dimensions such as quasi-1D nanotubes.

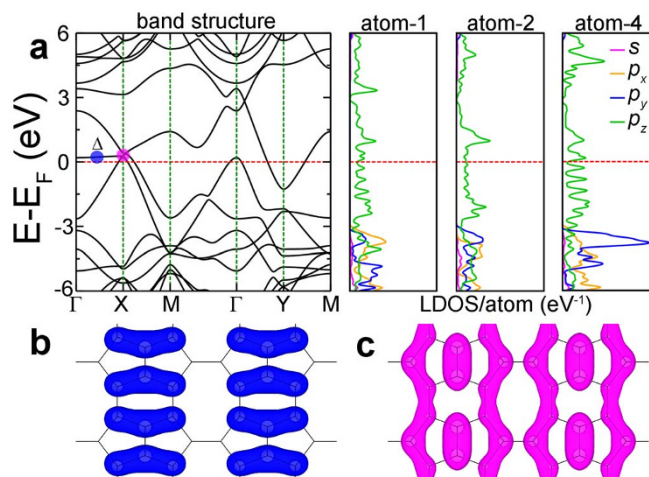


Figure 3 | Electronic properties of the pentahexoctite sheet. (a) Band structure of the pentahexoctite sheet with the angular momentum resolved density of states (LDOS). Fermi level E_F is set to 0 (red-dashed line). (b) and (c) The band decomposed charge densities at Δ (blue-colored circle in (a)) and X (magenta-colored circle in (a)) points, respectively. The isosurface value was set at $0.005 \text{ e}/\text{\AA}^3$.

We generate the nanotubes by rolling the pentahexoctite sheet. The chiral vector, \mathbf{C}_h and its corresponding translation vector, \mathbf{T}_h are shown in Fig. 1(a). Unlike graphene, the chiral vectors span from 0° to 90° . The chirality of a tube is defined by:

$$\mathbf{C}_h = m\mathbf{a}_1 + n\mathbf{a}_2 \quad (5)$$

where, m and n are the chiral indices. We restrict our study to achiral tubes, $(m,0)$ and $(0,n)$, formed by rolling the sheet along \mathbf{a}_1 and \mathbf{a}_2 , respectively.

The tubes are stable upon complete relaxation, as shown in Figs. 4(a) (0,8) and (b) (8,0) tubes. The relaxation of the tubes is chirality-dependent. While in the $(0,n)$ nanotubes, the buckling is observed at the pentagonal sites, the $(m,0)$ tubes are seamless. The buckling in the $(0,n)$ tubes originates from two factors: higher curvature of $(0,n)$ tubes as well as larger δ_{avg} ($\approx 1.119^\circ$ for (0,8)) in $(0,n)$ compared to the $(m,0)$ ($\approx 0.107^\circ$ for (8,0)) ones. We study the implications of the difference in the geometry on the stability of these tubes. Figs. 4(c) and (d), show the phonon dispersion of the $(0,n)$ and $(m,0)$ tubes, respectively. As a consequence of the local buckling in $(0,n)$ tubes, the TA1 and TA2 modes (right insets of Fig. 4(c)) get softened (zoomed-in version in the left inset of Fig. 4(c)). However, for the $(m,0)$ tubes, due to the seamless geometry, there is no mode-softening (Fig. 4(d)). With the decrease (increase) in the $(0,n)$ tube's curvature (diameter), the mode softening decreases eventually vanishing at the zero curvature (infinite diameter) limit, i.e., the sheet.

In order to further assess the mechanical stability, we calculate the in-plane stiffness (C_s) and the Poisson's ratio (ν). C_s for $(0,n)$ tubes (Table 1) are lower than the $(m,0)$ ones (Table 2), as a direct consequence of this mode softening. The increase in C_s with decrease in curvature (Table 1) reflects the trend obtained for the phonon mode-softening. On the contrary, there is no significant variation in C_s with increase in $(m,0)$ tube diameters (Table 2). The Poisson ratio (ν) was evaluated from the negative ratio of the radial strain (ϵ_{radial}) to the axial strain (ϵ_{axial}). The variation of ν with diameter, is the same for both the cases (Tables 1 and 2).

Flexural rigidity (D) is a very important mechanical parameter that provides a measure of the resistance of the sheet to bending to form a tube. It establishes the relationship between the tube's equilibrium energy (E_{eq}) and its curvature ($1/d^2$) via the following equation³⁴:

$$E_{\text{eq}} = A + \frac{2D}{d^2} \quad (6)$$

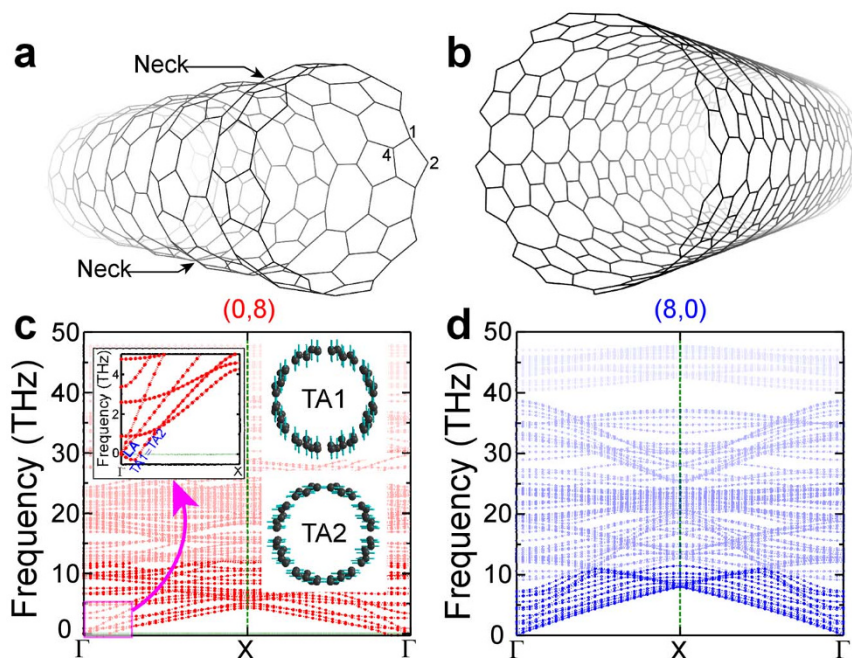


Figure 4 | Geometry and mechanical stability of the $(0,n)$ and $(m,0)$ nanotubes. (a) and (b) Relaxed geometries of the nanotubes with chiralities $(0,8)$ and $(8,0)$. (c) and (d), the corresponding phonon dispersions. Atoms on which the DOS is projected, to calculate the electronic properties of $(0,n)$ tubes, are numbered in (a). Left inset of panel (c) shows a zoomed version of the acoustical branches with the degenerate softened phonon modes near Γ , while the remaining insets, the direction of atomic vibrations (blue arrows) corresponding to these softened modes.

E_{eq} is plotted against the curvature as shown in Fig. 5(a). The intercept A gives the energy per atom of the pentahexoctite sheet, whereas half of the slope gives the value of flexural rigidity (D). The D values for the $(m,0)$ and $(0,n)$ tubes, are $2.82 \text{ eV}\text{\AA}^2/\text{atom}$ and $1.56 \text{ eV}\text{\AA}^2/\text{atom}$, which are within a range of 30–61% of CNTs³⁵. Hence, despite the presence of anisotropy in the sheet, the sheet still shows a high resistance to bending.

Raman spectroscopy is a very important tool for probing the properties of CNTs. One of the most important, of the many Raman active modes, is the low-frequency radial breathing mode (RBM) or the A_{1g} mode, given by the following equation^{35–38}:

$$\omega_{\text{RBM}} = \frac{1}{2\pi cR} \sqrt{\frac{C}{\rho_A(1-\nu^2)}} \quad (7)$$

where, R , ρ_A , and c are the radius, the mass density per cross-sectional area of the tube, and the speed of light (to convert to the spectroscopic unit of cm^{-1}), respectively. It is possible to characterize the tubes derived from the pentahexoctite sheet by calculating ω_{RBM} . ω_{RBM} for pentahexoctite tubes were calculated and plotted against the inverse of the radius, as shown in Fig. 5(b). The inset in this figure, illustrates RBM for the $(8,0)$ tube. A linear variation in ω_{RBM} is observed which is in agreement with the results obtained for CNTs^{36,39}. The values of ω_{RBM} were subsequently fitted to the equation:

$$\omega_{\text{RBM}} = A_0 + \frac{A_1}{R} \quad (8)$$

to obtain the spectroscopic constants A_0 and A_1 : 8.04 cm^{-1} and $1081.97 \text{ cm}^{-1} \text{\AA}$ for $(m,0)$ tubes, and 40.29 cm^{-1} and $774.57 \text{ cm}^{-1} \text{\AA}$ for $(0,n)$ tubes. These spectroscopic constants provide a reliable method for theoretically predicting the RBM frequency for any given diameter of the tube. ω_{RBM} values obtained from continuum mechanics were further verified by DFPT calculations for both $(0,8)$ and $(8,0)$ tubes.

Turning to the electronic properties of the tubes, we find that the $(m,0)$ and $(0,n)$ tubes exhibit different electronic properties, due to the anisotropy in the parent sheet. Figs. 6(a) and (b) show the band structures and projected DOS (PDOS) of the $(7,0)$ and $(0,7)$ nanotubes, respectively. The presence of finite number of states at E_F (Figs. 6(a) and (b)), renders these tubes metallic. The flat bands of the $(0,7)$ tube resembles a portion of the band structure of the sheet along the Γ -X-M direction, whereas the highly dispersive bands of $(7,0)$, the Γ -Y-M direction. The band structure of the sheet is, therefore, ‘split’ depending on the chirality of the tubes. This unique splitting feature is not restricted to these two tubes but is observed in the entire family of $(0,n)$ and $(m,0)$ tubes. An interesting feature of the electronic structure of the $(0,n)$ tubes, is the presence of linear dispersive bands forming a Dirac cone at the X point. The band-decomposed charge densities are calculated for the flat band (colored

Table 1 | Mechanical stiffness values for $(0,n)$ family of nanotubes

Tube	$\frac{\partial^2 E(\epsilon)}{\partial \epsilon^2}$ (eV)	C_s (Nm ⁻¹)	ν	ω_{RBM} (cm ⁻¹)
(0,6)	36.06	208.64	0.203	251.79
(0,7)	36.72	212.47	0.216	218.83
(0,8)	42.28	244.59	0.179	204.24
(0,9)	41.59	240.63	0.249	182.70
(0,10)	43.03	248.93	0.182	164.83
$(0,\infty)$	51.75	299.40	-	-

Table 2 | Mechanical stiffness values for $(m,0)$ family of nanotubes

Tube	$\frac{\partial^2 E(\epsilon)}{\partial \epsilon^2}$ (eV)	C_s (Nm ⁻¹)	ν	ω_{RBM} (cm ⁻¹)
(6,0)	54.04	312.69	0.220	204.47
(7,0)	53.30	308.35	0.230	174.62
(8,0)	54.26	313.88	0.156	152.08
(9,0)	55.31	320.01	0.291	140.97
(10,0)	55.30	319.92	0.254	125.31
$(\infty,0)$	58.56	338.79	-	-

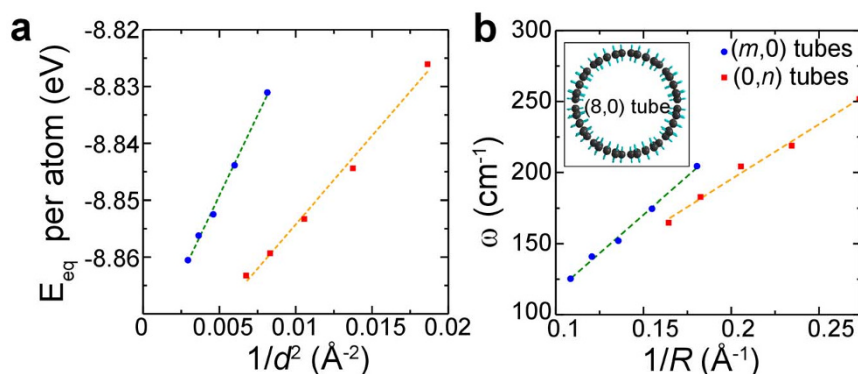


Figure 5 | Mechanical parameters of the nanotubes. (a) Equilibrium energy per atom (E_{eq}) of the tube vs. curvature ($1/d^2$) for both ($m,0$) (blue circles) and ($0,n$) (red squares) tubes. (b) The radial breathing mode (RBM) frequency (ω_{RBM}) of the ($m,0$) (blue circles) and ($0,n$) (red squares) tubes as a function of the inverse of their radii. The inset shows the RBM for the (8,0) tube. The green- and orange-dashed lines, in both (a) and (b), correspond to the linear fits of the ($m,0$) and ($0,n$) tubes respectively.

green in Fig. 6(c)), as well as the bands constituting lower, and upper Dirac cones (colored blue and red, respectively in Fig. 6(c)). As expected, the flat band shows a localized charge density. On the other hand, lower and upper cones originate from highly delocalized charge densities leading to linearly dispersive bands at the X point. Although the tubes are metallic, the band structures of the ($m,0$) and ($0,n$) tubes are quite different and very rich in features, and therefore, would lead to very interesting transport properties.

Conclusions

In summary, we propose a new sp^2 hybridized 2D allotrope of carbon, named as “pentahexoctite”. This sheet has a reduced Cmm symmetry with mechanical strength comparable with that of graphene. The band structure of the sheet is a very unique combination of flat as well as highly dispersive bands, consequently rendering it metallic. The difference in the nature of the bands along different directions would lead to the anisotropy in the electronic transport of the sheet. The band structure of the sheet ‘splits’ when the nanotubes with ($0,n$) and ($m,0$) chiralities, respectively, are rolled out of these sheets. In addition to the very rich and chirality-dependent electronic properties, the mechanical properties are also chirality-dependent. The absence of the negative frequencies in the phonon spectra along with comparatively lower energy with respect to the already existing 2D allotropes, indicates a strong possibility for this sheet to be realized experimentally.

Methods

All calculations were performed using first-principles density functional theory (DFT)⁴⁰ as implemented in the Vienna *ab initio* simulation package (VASP)^{41,42}. Projector augmented wave (PAW)^{43,44} pseudopotentials were used to represent the electron-ion interactions. The exchange and correlation part of the total energy was approximated by the generalized gradient approximation (GGA) using Perdew-Burke-Ernzerhof (PBE) type of functional⁴⁵. A unit cell of the sheet consists of eight atoms, with a vacuum of 15 Å added along the z -axis to avoid spurious interactions between the sheet and its periodic images. For integrations over the Brillouin zone, a well-converged Monkhorst-Pack (MP) k -point mesh⁴⁶ of $13 \times 21 \times 1$ (commensurating with the lattice vectors) was used. For tubes, a 15 Å vacuum was included in both, x and y directions, and well-converged MP k -meshes of $1 \times 1 \times 5$ and $1 \times 1 \times 7$ were used for ($m,0$) and ($0,n$) chiralities, respectively. Structural relaxation was performed using the conjugate-gradient method until the absolute value of the components of the Hellman-Feynman forces were converged to within 0.005 eV/Å. The convergence with respect to the energy cut-offs were performed and the default energy cut-off value of 400 eV was found to be sufficient. Phonon dispersions were obtained by using density functional perturbation theory (DFPT)⁴⁷ with a strict energy convergence criterion of 1×10^{-8} eV and an energy cut-off of 500 eV in order to obtain accurate forces.

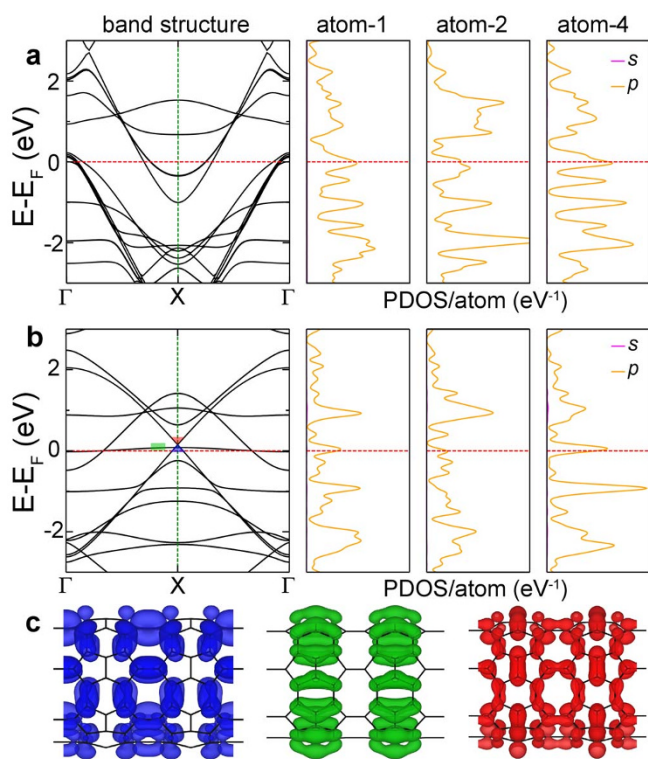


Figure 6 | Electronic properties of the ($0,n$) and ($m,0$) nanotubes. (a) and (b) Band structures and PDOS of atoms 1, 2, and 4 for the (7,0) and (0,7) nanotubes, respectively. Fermi level E_F is set to 0 (red-dashed line). (c) Indicates the band-decomposed charge densities corresponding to flat band (green color), as well as lower and upper Dirac cones (blue and red colors, respectively) at the X point. The isosurface value was set at $0.0011 e/\text{Å}^3$.

- Novoselov, K. S. *et al.* Two-dimensional gas of massless Dirac fermions in graphene. *Nature* **438**, 197–200 (2005).
- Geim, A. K. & Novoselov, K. S. The rise of graphene. *Nat. Mater.* **6**, 183–191 (2007).
- Enyashin, A. N. & Ivanovskii, A. L. Graphene allotropes. *Phys. Status Solidi B* **248**, 1879–1883 (2011).
- Baughman, R. H., Eckhardt, H. & Kertesz, M. Structure-property predictions for new planar forms of carbon: Layered phases containing sp^2 and sp atoms. *J. Chem. Phys.* **87**, 6687–6699 (1987).
- Narita, N., Nagai, S., Suzuki, S. & Nakao, K. Optimized geometries and electronic structures of graphyne and its family. *Phys. Rev. B* **58**, 11009–11014 (1998).
- Coluci, V. R., Braga, S. F., Legoas, S. B., Galvão, D. S. & Baughman, R. H. Families of carbon nanotubes: Graphyne-based nanotubes. *Phys. Rev. B* **68**, 035430 (2003).
- Yang, Y. & Xu, X. Mechanical properties of graphyne and its family - a molecular dynamics investigation. *Comput. Mater. Sci.* **61**, 83–88 (2012).



8. Zhou, J. *et al.* Electronic structures and bonding of graphyne sheet and its BN analog. *J. Chem. Phys.* **134**, 174701 (2011).
9. Cranford, S. W. & Buehler, M. J. Mechanical properties of graphyne. *Carbon* **49**, 4111–4121 (2011).
10. Malko, D., Neiss, C., Viñes, F. & Görling, A. Competition for graphene: Graphynes with direction-dependent dirac cones. *Phys. Rev. Lett.* **108**, 086804 (2012).
11. Kim, B. G. & Choi, H. J. Graphyne: Hexagonal network of carbon with versatile Dirac cones. *Phys. Rev. B* **86**, 115435 (2012).
12. Diederich, F. & Rubin, Y. Synthetic approaches toward molecular and polymeric carbon allotropes. *Angew. Chem. Int. Ed.* **31**, 1101–1123 (1992).
13. Li, G. *et al.* Architecture of graphdiyne nanoscale films. *Chem. Commun.* **46**, 3256–3258 (2010).
14. Long, M., Tang, L., Wang, D., Li, Y. & Shuai, Z. Electronic structure and carrier mobility in graphdiyne sheet and nanoribbons: Theoretical predictions. *ACS Nano* **5**, 2593–2600 (2011).
15. Song, Q. *et al.* Graphenylene, a unique two-dimensional carbon network with nonlocalized cyclohexatriene units. *J. Mater. Chem. C* **1**, 38–41 (2013).
16. Hudspeth, M. A., Whitman, B. W., Barone, V. & Peralta, J. E. Electronic properties of the biphenylene sheet and its one-dimensional derivatives. *ACS Nano* **4**, 4565–4570 (2010).
17. Konstantinova, E., Dantas, S. O. & Barone, P. M. V. B. Electronic and elastic properties of two-dimensional carbon planes. *Phys. Rev. B* **74**, 035417 (2006).
18. Boldi, A. M. & Diederich, F. Expanded radialenes: A novel class of cross-conjugated macrocycles. *Angew. Chem. Int. Ed.* **33**, 468–471 (1994).
19. Lange, T. *et al.* Hexakis(trimethylsilylethynyl)[3]radialene: A carbon-rich chromophore with unusual electronic properties. *Angew. Chem. Int. Ed.* **34**, 805–809 (1995).
20. Crespi, V. H., Benedict, L. X., Cohen, M. L. & Louie, S. G. Prediction of a pure-carbon planar covalent metal. *Phys. Rev. B* **53**, R13303–R13305 (1996).
21. Terrones, H. *et al.* New metallic allotropes of planar and tubular carbon. *Phys. Rev. Lett.* **84**, 1716–1719 (2000).
22. Stone, A. & Wales, D. Theoretical studies of icosahedral C₆₀ and some related species. *Chem. Phys. Lett.* **128**, 501–503 (1986).
23. Lahiri, J., Lin, Y., Bozkurt, P., Oleynik, I. I. & Batzill, M. An extended defect in graphene as a metallic wire. *Nat. Nano.* **5**, 326–329 (2010).
24. Chen, J.-H. *et al.* Controlled growth of a line defect in graphene and implications for gate-tunable valley filtering. *Phys. Rev. B* **89**, 121407 (2014).
25. Pop, E., Varshney, V. & Roy, A. K. Thermal properties of graphene: Fundamentals and applications. *MRS Bull.* **37**, 1273–1281 (2012).
26. Balandin, A. A. Thermal properties of graphene and nanostructured carbon materials. *Nat. Mater.* **10**, 569–581 (2011).
27. Liu, Y., Penev, E. & Yakobson, I. B. BallTran (Ballistic Transport Calculator). URL <https://sites.google.com/site/yuanyueliucms/codes> (2013). Date of access: 22/12/2013.
28. Lee, C., Wei, X., Kysar, J. W. & Hone, J. Measurement of the elastic properties and intrinsic strength of monolayer graphene. *Science* **321**, 385–388 (2008).
29. Lu, H. & Li, S.-D. Two-dimensional carbon allotropes from graphene to graphyne. *J. Mater. Chem. C* **1**, 3677–3680 (2013).
30. Zhao, M., Dong, W. & Wang, A. Two-dimensional carbon topological insulators superior to graphene. *Sci. Rep.* **3**, 3532; DOI:10.1038/srep03532 (2013).
31. Kotakoski, J., Krashennnikov, A. V., Kaiser, U. & Meyer, J. C. From point defects in graphene to two-dimensional amorphous carbon. *Phys. Rev. Lett.* **106**, 105505 (2011).
32. Meyer, J. C. *et al.* Direct imaging of lattice atoms and topological defects in graphene membranes. *Nano Lett.* **8**, 3582–3586 (2008).
33. Li, L., Reich, S. & Robertson, J. Defect energies of graphite: Density-functional calculations. *Phys. Rev. B* **72**, 184109 (2005).
34. Singh, A. K., Sadrzadeh, A. & Yakobson, B. I. Probing properties of boron α -tubes by *ab initio* calculations. *Nano Lett.* **8**, 1314–1317 (2008).
35. Kudin, K. N., Scuseria, G. E. & Yakobson, B. I. C₂F, BN, and C nanoshell elasticity from *ab initio* computations. *Phys. Rev. B* **64**, 235406 (2001).
36. Kürti, J., Kresse, G. & Kuzmany, H. First-principles calculations of the radial breathing mode of single-wall carbon nanotubes. *Phys. Rev. B* **58**, R8869–R8872 (1998).
37. Dresselhaus, M. S., Dresselhaus, G. & Saito, R. Carbon fibers based on C₆₀ and their symmetry. *Phys. Rev. B* **45**, 6234–6242 (1992).
38. Araujo, P. T. *et al.* Nature of the constant factor in the relation between radial breathing mode frequency and tube diameter for single-wall carbon nanotubes. *Phys. Rev. B* **77**, 241403 (2008).
39. Rao, A. M. *et al.* Diameter-selective raman scattering from vibrational modes in carbon nanotubes. *Science* **275**, 187–191 (1997).
40. Kohn, W. & Sham, L. J. Self-consistent equations including exchange and correlation effects. *Phys. Rev.* **140**, A1133–A1138 (1965).
41. Kresse, G. & Furthmüller, J. Efficiency of *ab initio* total energy calculations for metals and semiconductors using a plane-wave basis set. *Comput. Mater. Sci.* **6**, 15–50 (1996).
42. Kresse, G. & Furthmüller, J. Efficient iterative schemes for *ab initio* total-energy calculations using a plane-wave basis set. *Phys. Rev. B* **54**, 11169–11186 (1996).
43. Blöchl, P. E. Projector augmented-wave method. *Phys. Rev. B* **50**, 17953–17979 (1994).
44. Kresse, G. & Joubert, D. From ultrasoft pseudopotentials to the projector augmented-wave method. *Phys. Rev. B* **59**, 1758–1775 (1999).
45. Perdew, J. P., Burke, K. & Ernzerhof, M. Generalized gradient approximation made simple. *Phys. Rev. Lett.* **77**, 3865–3868 (1996).
46. Monkhorst, H. J. & Pack, J. D. Special points for brillouin-zone integrations. *Phys. Rev. B* **13**, 5188–5192 (1976).
47. Gonze, X. & Vigneron, J.-P. Density-functional approach to nonlinear-response coefficients of solids. *Phys. Rev. B* **39**, 13120–13128 (1989).

Acknowledgments

The authors thank the Supercomputer Education and Research Centre and Materials Research Centre, IISc, for providing the required computational facilities necessary for the above work.

Author contributions

B.R.S. and A.M. performed all the calculations and contributed equally. All the authors participated in writing of the manuscript. A.K.S. conceived, designed, and supervised the entire project.

Additional information

Competing financial interests: The authors declare no competing financial interests.

How to cite this article: Sharma, B.R., Manjanath, A. & Singh, A.K. *pentahexoctite*: A new two-dimensional allotrope of carbon. *Sci. Rep.* **4**, 7164; DOI:10.1038/srep07164 (2014).



This work is licensed under a Creative Commons Attribution-NonCommercial-ShareAlike 4.0 International License. The images or other third party material in this article are included in the article's Creative Commons license, unless indicated otherwise in the credit line; if the material is not included under the Creative Commons license, users will need to obtain permission from the license holder in order to reproduce the material. To view a copy of this license, visit <http://creativecommons.org/licenses/by-nc-sa/4.0/>